CRYSTAL GROWTH & DESIGN

Article

pubs.acs.org/crystal

Evolution of the *m*-Plane Quantum Well Morphology and Composition within a GaN/InGaN Core−Shell Structure

Pierre-Marie Coulon,*[,†] Shahrzad hosseini Vajargah,[‡] An Bao,[‡] Paul R. Edwards,[§] Emmanuel D. Le Boulbar,[†] Ionut Girgel,[†] Robert W. Martin,[§] Colin J. Humphreys,[‡] Rachel A. Oliver,[‡] Duncan W. E. Allsopp,[†] and Philip A. Shields[†]

[†]Department of Electronic and Electrical Engineering, University of Bath, Bath BA2 7AY, U.K.

[‡]Department of Materials Science and Metallurgy, University of Cambridge, Cambridge CB3 0FS, U.K.

[§]Department of Physics, SUPA, University of Strathclyde, Glasgow G4 0NG, U.K.

Supporting Information

ABSTRACT: GaN/InGaN core−shell nanorods are promising for optoelectronic applications due to the absence of polarization-related electric fields on the sidewalls, a lower defect density, a larger emission volume, and strain relaxation at the free surfaces. The core−shell geometry allows the growth of thicker InGaN shell layers, which would improve the efficiency of light emitting diodes. However, the growth mode of such layers by metal organic vapor phase epitaxy is poorly understood. Through a combination of nanofabrication, epitaxial growth, and detailed characterization, this work reveals an evolution in the growth mode of InGaN epitaxial shells, from a two-dimensional (2D) growth mode to three-dimensional (3D) striated growth without additional line defect formation with increasing layer thickness. Measurements of the indium distribution show fluctuations along the <10−10> directions, with low and high indium composition associated with the 2D and 3D growth modes, respectively. Atomic steps at the GaN/InGaN core−shell interface were observed to occur with a similar frequency as quasi-periodic indium fluctuations along [0001] observed within the 2D layer, to provide evidence that the resulting local strain relief at the steps acts as the trigger for a change of growth mode by elastic relaxation. This study demonstrates that misfit dislocation generation during the growth of wider InGaN shell layers can be avoided by using pre-etched GaN nanorods. Significantly, this enables the growth of absorption-based devices and light-emitting diodes with emissive layers wide enough to mitigate efficiency droop.

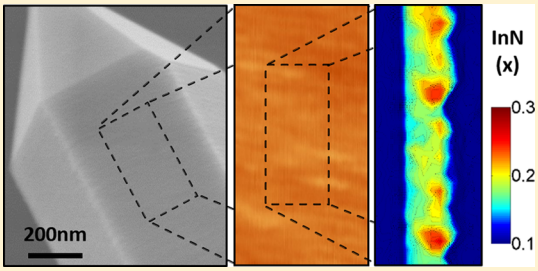

InGaN alloys and more generally III-nitride materials have been widely studied since their successful application in blue light-emitting diodes (LEDs) and laser diodes (LDs) in the early 90s.[1] With the possibility to tune the wavelength emission from 3.4 eV for GaN, to 0.7 eV for InN, InGaN quantum wells have been employed to achieve UV, blue, green, and white LEDs[2,3] and used for solar cells[4,5] or for water splitting.[6,7]

Despite commercialized devices with efficient near band edge emission, InGaN heterostructures grown on two-dimensional (2D) GaN layers still suffer from limitations such as poor crystalline quality due to the large lattice mismatch,[8,9] difficulty in growing high indium content layers,[10,11] pre-existing threading dislocations that adversely affect LED/LD performance,[8] and the introduction or expansion of V-defects and pits in the epitaxy.[8,9,12] The growth of thicker InGaN layers on GaN (or AlGaN) can lead to phase separation,[11,13] plastic relaxation, and elastic relaxation.[14,15] The result is the generation of new dislocations and three-dimensional (3D) growth that directly impact the InGaN emission properties.[8,9,16−18] Additionally, thick InGaN layers grown with the conventional *c*-plane orientation are seriously impacted by the quantum-confined Stark effect (QCSE), which results in poor emission efficiency due to the large spatial separation between electron and hole wave functions. The alternative of growing InGaN layers on the nonpolar and semipolar planes of wurtzite GaN to avoid the QCSE usually results in the formation of high densities of stacking faults that compromise the emissive properties,[19,20] unless grown on bulk GaN.

One way of circumventing these problems is to use a nanorod (NR) geometry that incorporates radial or axial InGaN heterostructures. Compared to 2D layers, GaN NRs allow an efficient strain relaxation[21] and can provide an almost defect-free core,[22] opening the possibility of higher indium incorporation with lower defect density, especially in the axial configuration.[23,24] In core−shell structures, InGaN growth on the nonpolar NR sidewalls not only eliminates the polarization-related electric fields but also leads to a larger emission volume for a given substrate footprint.[25] These advantages, as well as the potential to improve light extraction efficiency and

Received: August 29, 2016
Revised: December 22, 2016
Published: January 3, 2017

DOI: 10.1021/acs.cgd.6b01281
Cryst. Growth Des. 2017, 17, 474−482

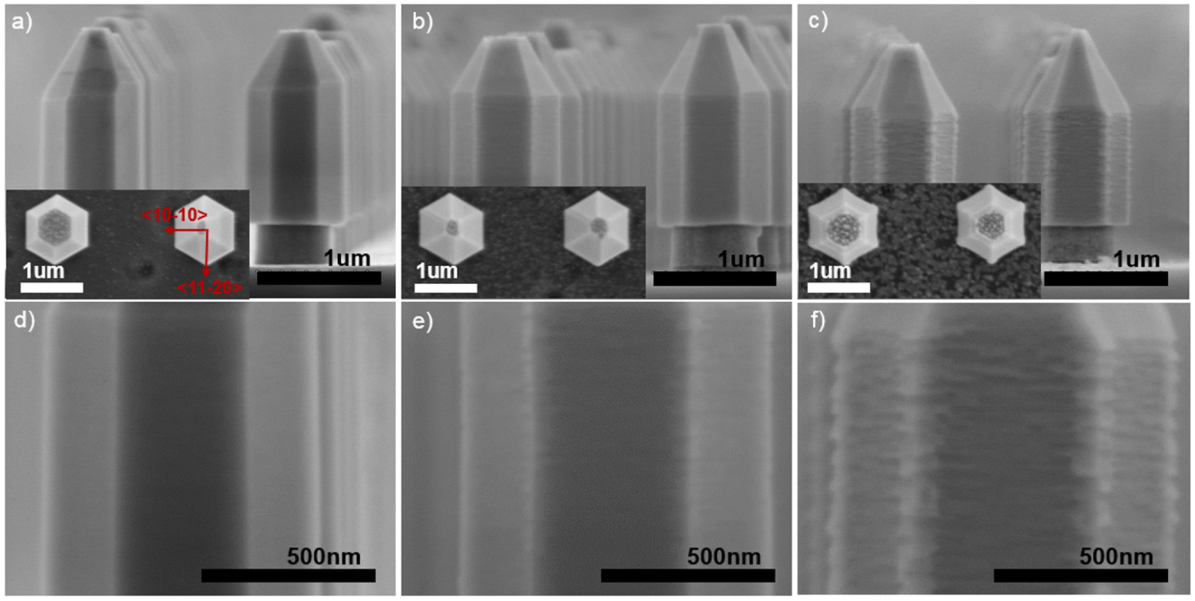

Figure 1. SEM pictures of GaN/InGaN uncapped core−shell structures grown by MOVPE for (a) 2 min, (b) 6 min, and (c) 18 min InGaN growth. The insets show plan-view SEM pictures of the same samples. High magnification SEM pictures of the *m*-plane facets for (d) 2 min, (e) 6 min, and (f) 18 min InGaN shell growth.

reabsorption, have therefore stimulated global interest in GaN/InGaN NR LEDs[26,27] and solar cells.[28]

The main focus of the GaN/InGaN core−shell literature to date has been on structures in which the InGaN layers are just 2−5 nm thick,[25,29−32] similar to the thicknesses of single or multiquantum well structures grown on *c*-plane GaN. However, the carrier densities in such narrow wells are high under normal LED operating conditions, with the consequence that efficiency droop is large. A particular motivation of this work is to grow and characterize wider InGaN layers on the nonpolar surfaces of core−shell structures in order to determine the scope to grow thicker active layers in GaN-based NRs for optoelectronic applications. The increase in the emissive volume of LEDs will have the effect of reducing the average carrier density in the emissive region for a given injection current and thus significantly mitigate efficiency droop.

Relevant work to date on GaN/InGaN core−shell NRs has focused on the optical uniformity of a wide (10 nm) InGaN single quantum well (SQW) on *m*-plane sidewalls, revealing nanoscale fluctuations in the InN mole fraction of up to 2.0−2.5 atom %.[33] This paper focuses on the evolution of the nanoscale fluctuations with increasing InGaN layer thickness, correlating changes in the nanoscale morphology with the local indium content. It is shown that *m*-plane miscut and related atomic layer steps in the faceted NR sidewalls can induce large fluctuations in the indium content and the morphology of nominally pseudomorphic InGaN thin films on a nanometer length scale. The results reveal wider implications for the growth of multicomponent alloy pseudomorphic epitaxial layers in core−shell structures and on their applications in optoelectronics.

RESULTS AND DISCUSSION

The InGaN shell layers used for this study were all grown on etched GaN NR arrays with a pitch of 2 μm, obtained by etching a GaN 2D layer down to the silicon substrate.[34] The use of top-down etching and regrowth gives rise to high uniformity of the NR array.[35,36] First, a metal organic vapor phase epitaxy (MOVPE) GaN regrowth step was performed to recover the *m*-plane and semipolar plane facets on the etched NR arrays. Next, an InGaN layer was grown under fixed growth conditions for a duration of 2, 6, or 18 min. A second set of three identical structures was grown, but this time with a GaN capping layer grown at 850 °C to create an InGaN/GaN double heterostructure. Further details of the overall NR fabrication process can be found in the Experimental Section and Supporting Information.

Figure 1 displays the evolution of the NR morphology as a function of the InGaN growth time. In each case the NR is defined by an envelope comprising six {10−10} *m*-plane facets, six {1−101} semipolar facets, and a truncated top (0001) *c*-plane facet. The high magnification scanning electron microscopy (SEM) images (Figure 1d,f) reveal a nanoscale evolution in the morphology of the *m*-plane facets with growth time. After 2 min growth the uncapped InGaN layer grown on the *m*-plane appears smooth without apparent roughness or change in morphology. After 6 min growth, surface roughness clearly appears along the entire length of the *m*-plane, with line features running parallel to the *c*-plane. After 18 min growth, these linear features are clearly revealed to be striations (Figure 1f). The same trend is observed when a GaN capping layer is grown over the InGaN layer.

For 18 min InGaN growth, cross-section (Figure 1f) and plan-view (inset in Figure 1c) SEM pictures clearly show a higher growth rate along the <11−20> direction, without {11−20} facets developing, compared to the <10−10> direction, indicating that group III species are preferentially incorporated on the edges between adjacent *m*-plane facets. The higher growth rate observed along <11−20> is likely due to the strain relaxation that occurs at the edges, enabling the larger indium atoms to be incorporated with less lattice dilation.[37]

The change in *m*-plane surface morphology observed as a function of the InGaN shell growth time was further examined by atomic force microscopy (AFM) experiments on NRs deposited onto a bare Si substrate by a scratching method. In addition, GaN faceted NRs (also referred to as 0 min InGaN)

DOI: 10.1021/acs.cgd.6b01281
Cryst. Growth Des. 2017, 17, 474−482

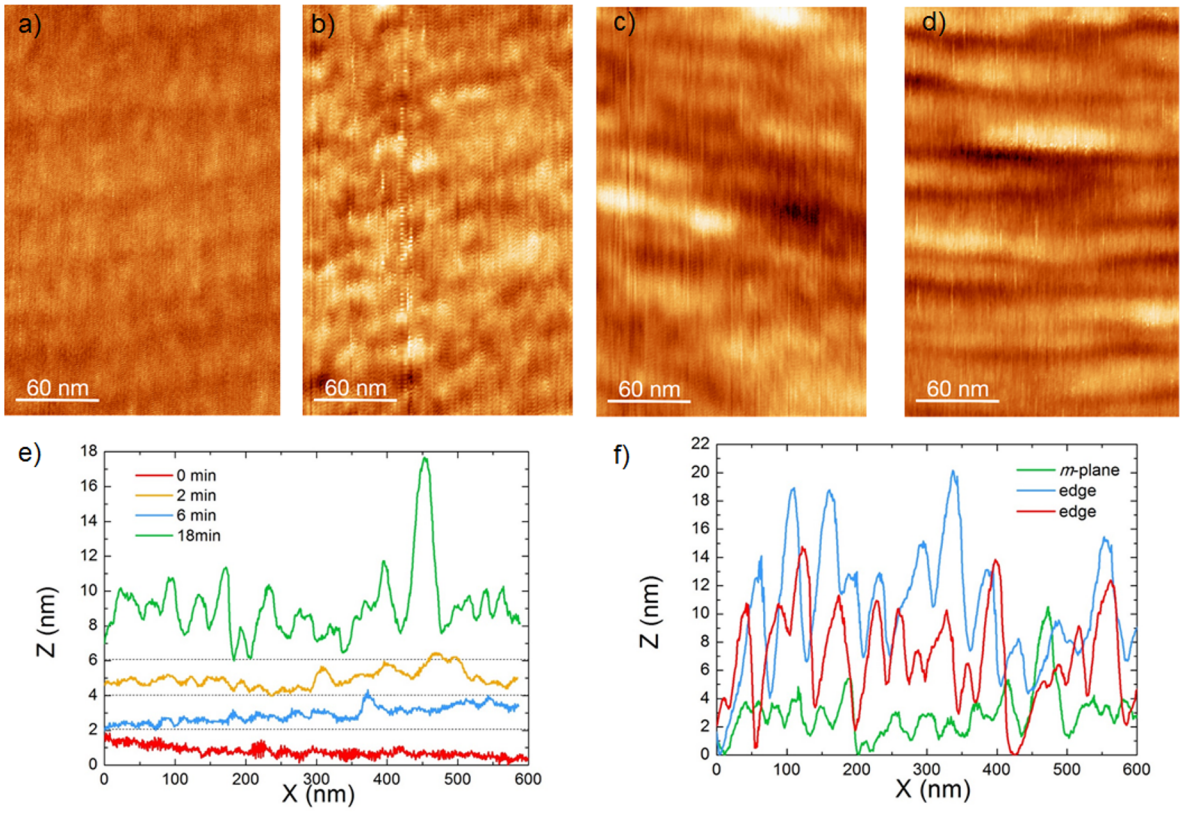

Figure 2. 300 × 200 nm^2 AFM scan of the *m*-plane for (a) GaN faceted NR (image height (*h*) = 2 nm), (b) 2 min (*h* = 2 nm), (c) 6 min (*h* = 3 nm), and (d) 18 min (*h* = 10 nm) uncapped InGaN shell growth time. AFM scans have been used to extract the RMS value of the *m*-plane avoiding any contribution of the edges. AFM line scans are traced along the *c*-axis to compare the height and spacing of the features or striations (e) in the middle of the *m*-plane as a function of the InGaN shell growth time and (f) between the middle of the *m*-plane and the edges for 18 min InGaN.

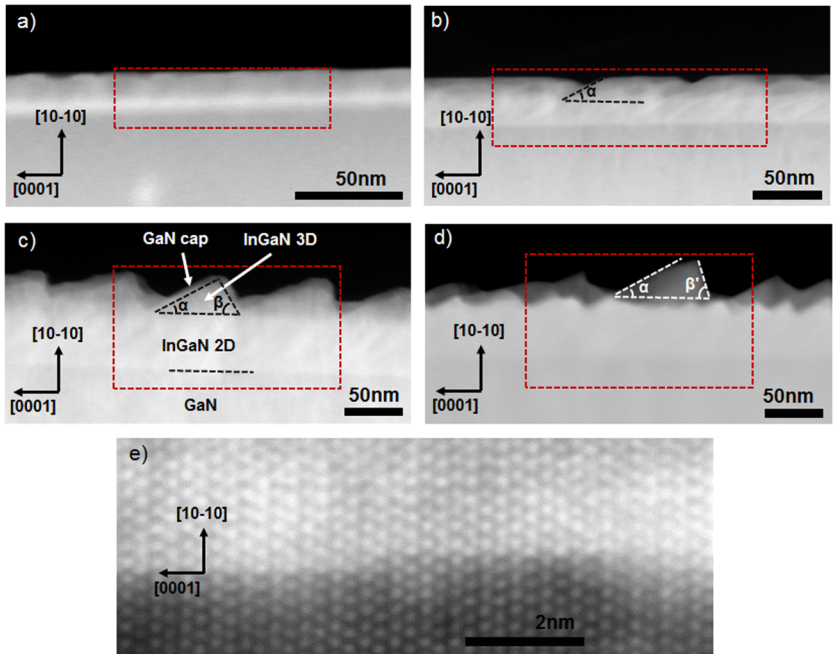

Figure 3. TEM pictures recorded along the [11−20] zone axis of GaN/InGaN core−shell structures grown by MOVPE with a GaN capping layer for (a) 2 min, (b) 6 min, (c) 18 min InGaN growth, and (d) for 18 min uncapped InGaN. The red dashed rectangle indicates the area where EDX spectra were acquired. The angle $\alpha = 29 \pm 1°$ corresponds to the average angle relative to the *m*-plane of the facet pointing toward [0001], whereas $\beta = 51 \pm 1°$ and β' $70 \pm 1°$ correspond to the different angles relative to the *m*-plane of the facet pointing toward [000−1]. (e) HRTEM picture of the GaN/InGaN interface recorded along the [11−20] zone axis.

DOI: 10.1021/acs.cgd.6b01281
Cryst. Growth Des. 2017, 17, 474−482

were also characterized to assess the initial surface morphology of the GaN *m*-plane sidewall. The RMS roughness value for each sample is extracted from the center of the *m*-plane (300 × 200 nm^2) to avoid any contribution of the edges.

The AFM height image of the GaN *m*-plane facet (Figure 2a), prior to the InGaN growth, exhibits quasi-periodic shallow step-like features running parallel to the *a*-axis with an RMS roughness of 0.184 nm. After 2 min InGaN growth (Figure 2b), similar features can be observed with a slightly increased roughness of 0.212 nm. With further growth, these linear features grow in height (i.e., along the <10−10> or *m*-direction) leading to the formation of striations and an increase in the RMS roughness to 0.403 nm for 6 min (Figure 2c) and 1.03 nm for 18 min (Figure 2d).

The initial quasi-periodic spacing of 20−40 nm between the step-like features observed for 0 min remains the same for longer InGaN growths up to the 18 min sample where merging/coalescence and local misalignment of the striation line features leads to an increase in the spacing, especially at the intersections of the *m*-planes where the spacing can reach up to 100 nm as the striations merge into larger structures (Figure 2f and Figure S2d of the Supporting Information). This is due to the faster growth rate and higher indium incorporation at these positions.

AFM line profiles are used to extract the height of the step-like features and striations from the middle of the *m*-plane facet, along the *c*-axis (see further details in Figures S2 and S3 of the Supporting Information) and are shown in Figure 2e for the various InGaN growth times. Measurements of the heights of the observed steps in AFM for the GaN faceted NR indicate that the vast majority consist of a single monolayer (ML) of GaN on the *m*-plane facet (see Figure S3). Then, as a function of the InGaN growth time, an increase in the height distribution size can be observed, up to 10 nm for the thickest InGaN in the middle of the *m*-plane facet, and up to 20 nm close to the edges (Figure 2f).

The features observed on the *m*-plane sidewalls of GaN faceted NRs are unambiguously ascribed to the presence of meandering steps. The fact that the size and the periodicity of these features remain the same after 2 min InGaN growth means that the initial InGaN layer formation occurs via a 2D step-flow growth mode. For longer growth, the change in size, alignment, and periodicity of the striations indicate that a significant perturbation at the surface takes place between 2 and 6 min InGaN growth, which is then exacerbated by continuing the InGaN growth to 18 min.

The surface morphology of the *m*-plane facet of the three InGaN capped samples and the 18 min InGaN uncapped sample was assessed by transmission electron microscopy (TEM), and the results are presented in Figure 3. In agreement with SEM and AFM observation, a change in morphology of the *m*-plane InGaN is observed with increasing growth time, from appearing essentially smooth for a 2 min growth time, evolving to a clearly roughened and striated surface after 18 min InGaN growth. Additional TEM color pictures recorded along the whole *m*-plane for the samples studied are shown in Figure S4 of the Supporting Information. The GaN capping layer (grown for 5 min) is conformal with the InGaN and has the same morphology and roughness. The increase of roughness with growth time seen on the SEM and AFM data can be correlated in the TEM images: the striations observed in the SEM and AFM images for the 6 min InGaN growth in Figures 1b and 2c are associated with the formation of new inclined facets that delineate sharply defined prismatic structures after 18 min InGaN growth (Figure 3c,d). After 6 min InGaN growth, the facets of the striation match to an *m* (1−101) plane (α in Figure 3b,c), whereas after 18 min, the facet pointing toward [000−1] gradually evolves to a (11−24) or (1−105) plane (respectively β and β' in Figure 3c,d).

An estimation of the InGaN SQW thickness can be obtained from the difference in GaN and InGaN contrast in the TEM images along the [10−10] direction, being 8 ± 1 nm and 20−24 ± 1 nm for the 2 and 6 min growth, respectively. Because of the emergence of the new facets after 6 min, the interface between the InGaN SQW and the GaN capping layer is no longer sharp, which leads to a thickness variation along the *m*-plane. In the case of the 18 min growth, an additional change in contrast along the [10−10] direction allows two layers to be distinguished: a bright two-dimensional (2D) layer having a thickness of 50 ± 2 nm and a dark three-dimensional (3D) striated layer having a variation in thickness up to 40−45 nm (Figure 3c,d) that compare well with the height and periodicity of the striations observed by AFM on the edges (Figure 2f). Compared to the 18 min capped growth, its equivalent uncapped sample (Figure 3d) has two distinct types of striation: 5−10 nm high undulations separated by 25−50 nm (bright contrast) and 30−45 nm high undulation with a 50−100 nm spacing. Thus, the TEM images involve not only the morphology of the *m*-plane but also the morphology of the edges.

An additional change in contrast can also be observed along the *c*-direction, within the InGaN 2D layer for all three InGaN growth times, but most noticeably in the 6 and 18 min grown samples (see also Figure S4b−d of the Supporting Information). Narrow darker regions inclined at 41 ± 2° ((11−23) plane) to the *m*-plane occur quasi-periodically. Since this change in contrast is observed only within the InGaN layer, it is not an artifact of the TEM preparation; rather, it is related to a real variation in the *m*-plane InGaN growth. These features will be discussed later after the determination of the indium composition within these layers.

No generation of defects (i.e., misfit dislocations or basal stacking faults) has been observed within the SQW in the NRs studied irrespective of the growth time. Complementary high-resolution TEM pictures have been performed at the GaN/InGaN interface and highlight the presence of atomic steps at the GaN/InGaN interface (Figure 3e), in agreement with the AFM observations on GaN faceted NRs (Figure 2a), but do not show the presence of misfit dislocations along the *m*-plane facet.

The formation of atomic steps on the *m*-plane facets of GaN NRs can be explained through understanding the fabrication process of the NRs. After the etching step that leads to the formation of the NRs, the lateral sidewalls of the NRs are slightly tapered; i.e., there is a small decrease of diameter from the bottom to the top.[35] While the GaN regrowth step will eventually reveal the slowest growing planes, such as the *m*-plane, the presence of atomic steps at the GaN/InGaN interface suggests that the recovery is not complete, leading to a +*c* *m*-plane miscut of 0.4 ± 0.01° (see further details on miscut calculation in Figure S3 of the Supporting Information). Detailed analysis of SEM data on similar samples reveals the same conclusion.[35]

The InGaN alloy composition within the InGaN SQWs was examined by energy-dispersive X-ray spectroscopy (EDX). Figure 4 shows typical EDX maps of the InN fraction measured

DOI: 10.1021/acs.cgd.6b01281
Cryst. Growth Des. 2017, 17, 474−482

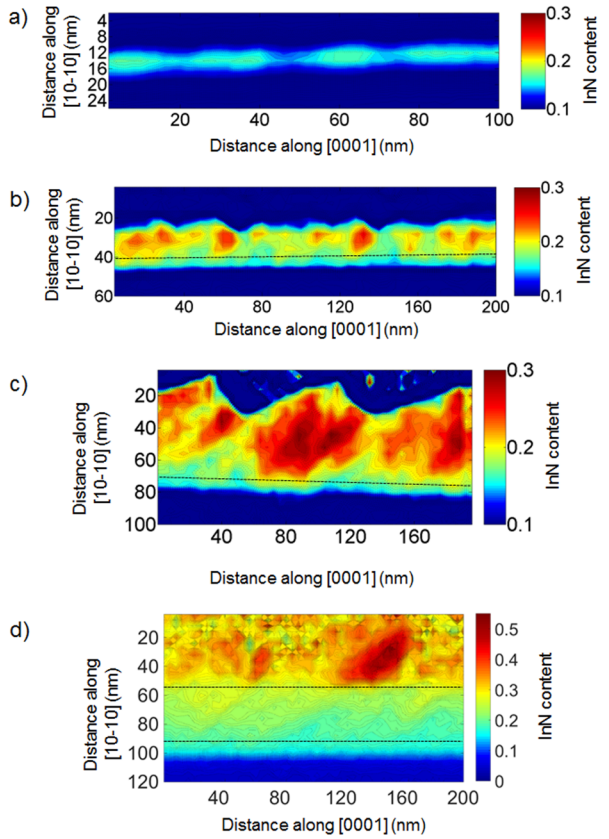

Figure 4. Indium content map obtained by EDX on capped GaN/InGaN core−shell structures grown by MOVPE for (a) 2 min, (b) 6 min, (c) 18 min InGaN growth, and (d) for 18 min uncapped InGaN growth. The position of the EDX maps acquired for each InGaN growth time is highlighted by a red dashed rectangle in Figure 3. A contour plot representation has been used to smooth the data and highlight the InN compositional fluctuations and changes in morphology of the InGaN shell layer (see Figure S4 of the Supporting Information for more details). The dashed lines highlighted in (b) and (c) highlight the initial strained 2D InGaN layer, whereas the dashed lines in (d) highlight both the first initial strained 2D layer and the second partially relaxed 2D layer.

on the *m*-plane facets for the InGaN-capped samples grown for 2, 6, and 18 min and the 18 min InGaN uncapped sample. Note that the color scale bar used for the EDX maps of the capped InGaN samples corresponds to a 10−30% variation in InN mole fraction content, whereas a 0−50% InN mole fraction scale bar was used for the uncapped InGaN sample. A clear increase in the volume averaged indium composition and its inhomogeneity can be seen with the increase in growth time. For each capped sample a maximum InN content of the InGaN layer has been calculated: 15% ± 2% for 2 min growth time, 25% ± 2% for 6 min, and 30% ± 2% for 18 min. Since all other growth parameters were kept constant, it can be inferred that the increase in InN content and its fluctuations in the InGaN layers derives solely from the transition from a quasi-2D to a 3D growth mechanism.

Focusing on the InN fluctuations, after 2 min InGaN growth (Figure 4a), EDX maps reveal quasi-periodical lateral fluctuations along the *c*-axis, with a difference in InN content of 2−3% and an average spacing of ∼20 nm between high and low InN content within the 8 nm wide InGaN SQW. The good correlation found between the quasi-periodicity of atomic steps observed on GaN facets along the *c*-axis in AFM (Figure 2a) and the quasi-periodical InN fluctuations detected along the *c*-axis after 2 min InGaN (Figure 4a) supports the assumption that the presence of atomic steps triggers InN fluctuations within the SQW. Indeed, atomic steps can enable the local accommodation of stress in pseudomorphic InGaN epitaxial layers by providing sites for preferential indium incorporation, either at the step itself due to the greater scope for bond relaxation[38,39] or by introducing a species-dependent Ehrlich−Schwöbel barrier (ESB) that inhibits, for example, the flux of In atoms perpendicular to the steps in the growing surface.[40] Since the InGaN growth adopts a step-flow growth mode between 0 and 2 min, as indicated by AFM characterization, it follows that after the deposition of each InGaN monolayer, preferential incorporation of indium will occur at or near the step edge, where the inherent strain induced due to the large atom size can be relaxed by displacing its lattice site. This is similar to what is observed in InGaN planar growth where it is suggested that adsorbed indium atoms migrate to the dilatational strain field of a dislocation core,[41] or more generally, that the kinetic mechanism of inhomogeneity formation is coupled to surface morphology.[42]

With the increase of growth time to 6 min (Figure 4b), two InGaN layers can now be distinguished along the [10−10] direction: first, a continuous inner layer of 8 nm of relatively homogeneous InN content (delineated by a dashed line in Figure 4b), and with a InN fraction of ∼15% similar to that observed after 2 min; and second, an outer layer characterized by lateral fluctuations in InN content of 10% with faceted regions of InN content up to 25%. The InN fluctuations again occur quasi-periodically with an average spacing of 20 nm. It is striking that the average lateral spacing of the InN content after 6 min is not only in good agreement with the striation spacing observed in AFM, but also similar to the lateral InN fluctuation average spacing estimated after 2 min. It is very likely that the high and low InN content variation of 2−3% seen after 2 min InGaN growth has created a sufficient perturbation, via elastic strain relaxation, to initiate the nucleation of others facets on the *m*-plane. Such facets, which look like islands for 6 min growth, will lead to a relaxed area where a favorable binding of indium atoms occurs,[17,18,38,42] explaining the higher indium content of the outer faceted InGaN layer compared to the inner layer. In InGaN *c*-plane growth the formation of 3D islands, occurring via elastic strain relaxation, will induce higher indium incorporation, particularly near the top of the island where the material is the most relaxed, leading to high indium fluctuation.[17,18] The growth mode commonly ascribed to the formation of 3D islands or nanostructures such as quantum dots is the Stranski−Krastanov (SK) growth mode where first, a 2D pseudomorphic strain layer with a low indium content due to the strain compositional pulling effect is grown,[16] followed by 3D elastically relaxed growth favorable to higher indium incorporation. In the present case, a first layer with low indium content is observed, followed by the formation of a 3D striated layer composed of new facets, with higher indium content. As such, the InGaN growth mode on the *m*-plane facets of the fabricated NRs is similar to SK growth, except for being triggered by atomic layer steps. Unlike the nucleation of a 3D island geometry in *c*-plane growth of InGaN/GaN QWs, which is mainly due to the existence of a biaxial strain, the presence of atomic steps leads to the formation of 3D striations preferentially aligned along the *a*-axis.

As growth proceeds, there is a competition between the remaining *m*-plane and other facets. After 18 min, well-defined

DOI: 10.1021/acs.cgd.6b01281
Cryst. Growth Des. 2017, 17, 474−482

facets other than the *m*-plane are obtained, indicating that the growth proceeded via a self-limiting process, with the *m*-plane growing faster than the (1−101) and (11−24) or (1−105) facets. Similar to that observed after 6 min, the EDX map (Figure 4c) reveals an initial layer of 8−10 nm with an InN content similar to that observed after 2 and 6 min (delineated by a dashed line), followed by a layer having higher InN content area up to 25−30%. The latter is clearly located in the upper part of the InGaN layer with a periodicity that matches that observed along the edges by AFM.

The EDX map of the 18 min InGaN uncapped sample (Figure 4d) reveals a clear delineation between the initial 2D InGaN layer having a thickness of 50 nm and the 3D striated features, in good correlation with TEM (Figure 3d). Within the 2D InGaN layer, it is possible to distinguish two layers (delineated by dashed lines in Figure 4d): a first layer of 8−10 nm with an InN content similar to that observed for the other samples, followed by a second layer of 40 nm thickness having a higher InN content and slightly higher lateral fluctuations of 5−10%. The lateral fluctuations propagate at an average angle relative to the *m*-plane of 41 ± 2° ((11−23) plane), in good correlation with the inclined regions of high and low contrast observed within the 2D InGaN layer in Figure 3b,c, which can consequently be ascribed to fluctuations in the InN content. For the outer 3D striated InGaN layer, the InN content of the small and large size striation features (Figure 3d) associated with the middle of the *m*-plane and their edges can be extracted, having respectively a maximum content of 30% and 50%. It is worth pointing out that without any GaN capped layer, the maximum InN content grown on the edges is almost equal to the molar ratio of TMIn injected in the vapor phase (45%). Therefore, the observed difference in the maximum InN content noticed between GaN capped and uncapped InGaN growth, added to the difficulty in correlating the thickness of the 2D and 3D InGaN layer between TEM and EDX acquisition for the capped sample, could suggest that desorption or In−Ga inter diffusion of species takes place during the GaN cap growth.

The observation by EDX of a 2D and 3D layer in the thick InGaN sample is indubitable and correlates with the TEM observations. The increase in thickness of the 2D InGaN layer with the growth time could result from strain being elastically released through the formation of new facets (striations), with the effect that epitaxial growth occurs simultaneously in the 3D striations and the 2D layer, the latter acting like a wetting layer.

These results highlight a difference in the relaxation mechanism between InGaN shells grown on GaN NRs formed by top-down etching and regrowth and NRs formed by selective area growth (SAG). A study of the strain state of InGaN shells grown on SAG NRs with synchrotron X-rays showed that the strain is gradually relaxed via misfit dislocations.[43] In our case, no misfit dislocations are observed in HRTEM images of the GaN/InGaN interface with the strain elastically relaxed. This difference could be due to the lower density of atomic steps present on SAG NRs, which if present would initiate the accommodation of strain and elastic relaxation via 3D growth rather than plastic relaxation via the introduction of misfit dislocations.

The impact on the luminescent properties of the InGaN shell change in morphology and indium content with growth time was measured by room temperature high resolution cathodoluminescence (CL) spectroscopy.[44] CL spectra were acquired at the center of the *m*-plane facet with a 100 × 150 nm area fast scan. Figure 5 displays the CL spectra of the 2, 6, and 18 min growths for four different accelerating voltages in the range 1.5−10 kV, in order to probe different depths into the sample.

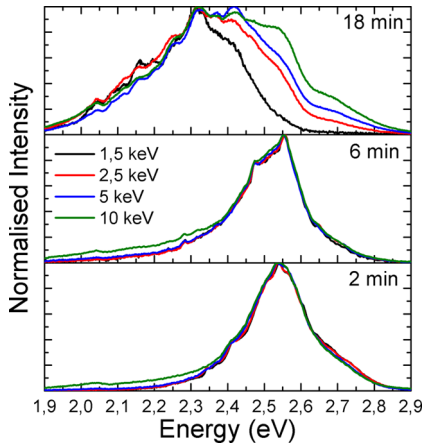

Figure 5. Cathodoluminescence spectra acquired at electron acceleration voltages of 1.5, 2.5, 5, and 10 kV for the 2 min (bottom pane), 6 min (middle pane), and 18 min (upper pane) capped GaN/InGaN core−shell structures. The different voltages lead to different penetration depths of the excitation within the sample.

For accelerating voltages of 1.5 kV, the electron beam penetration depth is ∼15 nm,[45] which is sufficient to penetrate the entire ∼8 nm thickness of the *m*-plane 2D InGaN layer grown for 2 min having an emission peak centered at 2.55 eV (lower pane of Figure 5). With increasing accelerating voltage, the peak position and full width at half-maximum remains almost unchanged. Thus, the emission peak centered at 2.55 eV only derives from the initially grown 2D pseudomorphic InGaN layer. The CL spectra of the ∼22 nm thick 6 min InGaN growth follow the same trend with increasing the accelerating voltage, with the main emission peak still centered at 2.55 eV (central pane of Figure 5). However, a small but perceptible increase in the relative intensity of the low energy tail compared with the main emission peak is observed, which, when comparing with TEM and EDX observations, correlates with a nascent stage of the formation of indium-rich 3D striations in the upper part of the 2D InGaN layer.

Unlike the 2 and 6 min InGaN growth, the CL spectra of the 18 min InGaN growth, displayed in the upper panel of Figure 5, show a clear dependence in the CL emission with increasing the accelerating voltage. For 1.5 kV, a broad emission peak centered at 2.32 eV with a higher energy shoulder at 2.42 eV dominates the spectra, whereas no emission peak can be found at 2.55 eV. By gradually increasing the accelerating voltage, the shoulder at 2.42 eV becomes a clearly resolved feature along with the higher energy shoulder corresponding to the 2.55 eV emission peak. Whereas the low 1.5 kV accelerating voltage is insufficient to excite the 2D InGaN layer, the 10 kV electron beam penetration depth of ≈50−60 nm is sufficient to excite the full width of the 18 min InGaN layer. Therefore, by correlating depth-resolved CL spectroscopy with AFM, TEM, and EDX observations for the 18 min InGaN growth, the 2.55 eV emission is unambiguously ascribed to the low indium content 2D pseudomorphic InGaN layer, the low energy 2.32 eV emission is related to the high indium content of the 3D relaxed striated InGaN layer, and the middle energy 2.42 eV

DOI: 10.1021/acs.cgd.6b01281
Cryst. Growth Des. 2017, 17, 474−482

emission can be associated with a 2D InGaN partially relaxed wetting layer having an intermediate indium content.

The CL spectroscopy data thus confirm the compositional differences between the initial 2D layer and the relaxed 3D striations found by EDX and further reveal a tendency for the volume-averaged indium content of the 3D striated features to increase with growth time.

CONCLUSION

In summary, the underlying growth mechanism of a thick InGaN shell grown on GaN NRs formed by combined top-down etching and regrowth has been described and explained through a correlation between the observed change of the InGaN morphology and composition. Combined AFM, TEM, and EDX evidence shows that the presence of quasi-periodic atomic steps along the *c*-axis of the *m*-plane GaN facets of the NRs induce preferential incorporation of species at or near the step edges, leading to lateral fluctuations in InN content along the *c*-axis. By adopting a step growth mode, the indium fluctuations build up, and strain inhomogeneity is induced within the InGaN layer. At a critical thickness, the strain is not gradually and homogeneously relieved through the formation of misfit dislocations, but instead inhomogeneously relieved through elastic relaxation and the formation of new facets, resulting in nanoscale quasi-periodic striations along the *c*-axis. The change in morphology subsequently leads to a higher variation in the indium incorporation between the remaining *m*-plane and the new inclined facets, with the InGaN 2D layer acting like a wetting layer. The as-grown thick InGaN consists of several sublayers with distinct compositions and strain states: a thin epitaxially strained 2D layer of low InN mole fraction having a slight fluctuation in mole fraction; a second, thicker, partially relaxed 2D layer of higher InN mole fraction and larger fluctuation; and finally, an upper relaxed section comprising strongly faceted striations of much higher InN mole fraction due to a more favorable binding of In atoms on the (1−101) and (11−24) planes. As such, this work shows that the indium composition and indium lateral fluctuations of the InGaN layer can be controlled by tuning the frequency of atomic steps on the NR sidewalls. With a combined top-down etching and regrowth fabrication process, this can be achieved through a judicious choice of NR etch profile and duration of GaN facet recovery growth to control the *m*-plane miscut along the +*c* axis. The density of the atomic steps could influence the critical thickness at which the strain relaxation process takes place, potentially allowing for the growth of thicker smooth InGaN layers without new dislocations forming, and opening the possibility of growing light emitting diodes with emissive layers wide enough to mitigate efficiency droop. In addition, the growth of thicker striated InGaN layers having no defects and a broader indium composition range would be valuable for absorption-based devices.

EXPERIMENTAL SECTION

Top-Down Fabrication Process. A nickel-based metal mask of 200 nm was created on a GaN on silicon template using a nanoimprint lift-off technique, resulting in a hexagonal array of metal dots of ∼510 nm diameter with a 2000 nm pitch. Subsequently, the GaN 2D layer was etched into the silicon to achieve a GaN/AlN/Si NR array (Figure S1a). The etching was performed in an inductively coupled plasma (ICP) dry etch system (Oxford Instruments System 100 Cobra) using the following recipe: a Cl_2 flow of 50 sccm, an Ar flow of 10 sccm, 120 W RIE power, 800 W ICP source power, 9 mTorr and 150 °C.

Regrowth Process. To promote growth on the NR sidewalls only, the underlying Si was protected from regrowth by passivation achieved by the formation of SiN_x on the exposed Si by an in situ MOVPE nitridation step at 950 °C. MOVPE GaN regrowth faceting was subsequently performed during 6 min at 900 °C, 100 mbars with 8 sccm in TMGa flow rate, and 2800 sccm in NH_3 flow rate (V/III ratio of 3865) to recover the {10−10} nonpolar and {1−101} semipolar facets (Figure S1b). Then, a first set of three different InGaN SQW thickness was grown for 2, 6, and 18 min at 700 °C, 300 mbars, 9 sccm in TMGa flow rate, 360 sccm in TMIn flow rate (the molar ratio of TMIn in the vapor phase was kept constant at 45% throughout the growths) and 5000 sccm in NH_3 flow rate (V/III ratio of 3430) without any GaN cap layer. Finally, the same set of growth was performed for three different times with the same InGaN SQW growth conditions, but this time with a GaN cap layer grown at 850 °C, 100 mbars, 9 sccm in TMGa flow rate, and 5000 sccm in NH_3 flow rate (V/III ratio of 6135).

AFM Characterization and Processing. The as-grown GaN and GaN/InGaN NRs samples were mechanically removed from the Si substrate and dispersed on a host Si substrate. The NRs were then carefully located within a SEM prior to AFM measurements to ensure that the studied NRs were lying flat on the substrate.

Tapping mode was used for all the AFM measurements. Line flattening on the selected areas of interest was performed to obtain the AFM height image of the *m*-plane facet for the GaN faceted NRs and the three uncapped InGaN samples, as illustrated in Figure S2. The RMS roughness value for each sample was extracted from the center of the *m*-facet to avoid any contribution of the apexes, as illustrated in Figure S2. The images to calculate RMS roughnesses are the same size and have all undergone line flattening. The height and periodicity of the features or striations were extracted via AFM line scans traced along the *c*-axis.

TEM and EDX Characterization. The samples for TEM observations and EDX measurements were prepared by a tripod polishing method using an Allied Tech Multiprep unit. Specimens were then ion-milled with a Gatan Precision Ion Polishing System (PIPS) using 1.5−5 keV argon ions for further thinning and removing the residue of polishing contamination from the specimens.

Samples for HRTEM were prepared by a dual beam focused ion beam milling using a FEI Nova 200 NanoLab high resolution field emission gun scanning electron microscope (FEGSEM) with precise focused ion beam (FIB) etch and deposition capabilities. The nanorods were protected by a platinum layer prior to etching to reduce the damage that could occur with the use of an ion beam system.

NRs shown in Figure 4a−d (same in Figure S3a−d) were prepared by a tripod polishing method, whereas the NR shown in Figure 4e was prepared using a focused ion beam.

The low magnification TEM investigations were performed using a FEI Tecnai Osiris fitted with high brightness field emission gun (XFEG). Experiments were carried out at an accelerating voltage of 200 kV and a beam current of 0.5 nA.

The HRTEM observations were performed using a FEI Titan3 Themis 300 fitted with high brightness XFEG with S-TWIN objective lens and monochromator (energy spread approximately 0.25 eV).

Energy dispersive X-ray spectroscopy analyses were carried out using an FEI Tecnai Osiris TEM. This microscope was equipped with XFEG and Super X system EDX detectors. This detector comprises 4 Bruker silicon drift detectors (SDD) arranged symmetrically around the optic axis of the microscope for high collection efficiency and high count rate. Spectrum images were acquired at a spatial sampling of 2 nm/pixel or 4 nm/pixel and 200 ms/pixel dwell times with a probe current of approximately 0.5 nA, at an accelerating voltage of 200 kV. Using principal component analysis (PCA) and independent component analysis (ICA) (implemented in HyperSpy47), two independent and uncorrelated components were identified in the spectrum images. The first component contains Ga and N X-ray peaks and the second component contain Ga, In, and N X-ray peaks. To obtain the composition of the InGaN shell, the intensities of Ga K_α and In L_α peaks were quantified using the Cliff-Lorimer method and

DOI: 10.1021/acs.cgd.6b01281
Cryst. Growth Des. 2017, 17, 474−482

the *k*-factor provided by the manufacturer of the EDX system (Bruker). The errors were also estimated from Poisson statistics. The ICA technique is capable of differentiating true spectra from the underlying noise efficiently, and, as a result, noisy spectra can be tolerated. Using the ICA technique, the required sample beam dose was therefore significantly minimized without compromising the accuracy of quantification.

CL Characterization. Cathodoluminescence spectroscopy was carried out at room temperature in a modified FEI Quanta 250 field emission SEM with various accelerating voltages. Light was collected using an NA0.28 reflecting objective with its axis perpendicular to the electron beam and focused directly to the entrance of the spectrograph using an off-axis paraboloidal mirror. We used a 125 mm focal length spectrograph with a 600 lines/mm grating and 50 μm entrance slit, coupled to a cooled electron multiplying charge-coupled device (EMCCD) detector.

■ ASSOCIATED CONTENT

Supporting Information

The Supporting Information is available free of charge on the ACS Publications website at DOI: 10.1021/acs.cgd.6b01281.

Additional pictures on GaN/InGaN core−shell NR fabrication process, AFM acquisitions and processing, TEM pictures and EDX data processing treatment (PDF)

■ AUTHOR INFORMATION

Corresponding Author

*E-mail: P.Coulon@bath.ac.uk.

ORCID

Pierre-Marie Coulon: 0000-0002-9120-7554

Duncan W. E. Allsopp: 0000-0003-4197-9852

Present Address

Department of Electronic and Electrical Engineering, University of Bath, BA2 7AY, UK

Author Contributions

P.-M.C. and E.D.B. conceived the experimental work, supervised by P.A.S. and D.W.E.A. P.-M.C. carried out the nanorod fabrication, MOVPE growth experiment, and SEM characterization. A.B. and R.A.O performed the AFM characterization. S.H.V. performed the TEM and EDX characterizations. P.R.E. and R.W.M. performed the CL characterization. All other authors contributed in analyzing and writing the results.

Notes

The authors declare no competing financial interest.

■ ACKNOWLEDGMENTS

The authors would like to thank OSRAM Opto Semiconductors GmbH for the provision of the GaN/silicon templates and acknowledge financial support from the European Union (FP7 Contract No.: 228999, "SMASH") and the EPSRC, UK via Grant No. EP/I012591/1 "Lighting the Future" and Grant No. EP/M015181/1, "Manufacturing nano-GaN". This publication is supported by multiple data sets, which are openly available here: http://doi.org/10.15125/BATH-00224.

■ REFERENCES

(1) Nakamura, S.; Mukai, T.; Senoh, M. *Appl. Phys. Lett.* **1994**, *64*, 1687.

(2) Nakamura, S. *Solid State Commun.* **1997**, *102*, 237.

(3) Mukai, T.; Nakamura, S. *Jpn. J. Appl. Phys.* **1999**, *38*, 5735.

(4) Jani, O.; Ferguson, I.; Honsberg, C.; Kurtz, S. *Appl. Phys. Lett.* **2007**, *91*, 132117.

(5) Dahal, R.; Pantha, B.; Li, J.; Lin, J. Y.; Jiang, H. X. *Appl. Phys. Lett.* **2009**, *94*, 063505.

(6) Fujii, K.; Karasawa, T.; Ohkawa, K. *Jpn. J. Appl. Phys.* **2005**, *44*, L543.

(7) Li, J.; Lin, J. Y.; Jiang, H. X. *Appl. Phys. Lett.* **2008**, *93*, 162107.

(8) Cho, H. K.; Lee, J. Y.; Yang, G. M.; Kim, C. S. *Appl. Phys. Lett.* **2001**, *79*, 215.

(9) Cho, H. K.; Lee, J. Y.; Kim, C. S.; Yang, G. M. *J. Appl. Phys.* **2002**, *91*, 1166.

(10) Thaler, G. T.; Koleske, D. D.; Lee, S. R.; Bogart, K. H. A.; Crawford, M. H. *J. Cryst. Growth* **2010**, *312*, 1817−1822.

(11) El-Masry, N. A.; Piner, E. L.; Liu, S. X.; Bedair, S. M. *Appl. Phys. Lett.* **1998**, *72*, 40.

(12) Chen, Y.; Takeuchi, T.; Amano, H.; Akasaki, I.; Yamada, N.; Kaneko, Y.; Wang, S. Y. *Appl. Phys. Lett.* **1998**, *72*, 710.

(13) Tessarek, C.; Figge, S.; Aschenbrenner, T.; Bley, S.; Rosenauer, A.; Seyfried, M.; Kalden, J.; Sebald, K.; Gutowski, J.; Hommel, D. *Phys. Rev. B: Condens. Matter Mater. Phys.* **2011**, *83*, 115316.

(14) Srinivasan, S.; Geng, L.; Liu, R.; Ponce, F. A.; Narukawa, Y.; Tanaka, S. *Appl. Phys. Lett.* **2003**, *83*, 5187.

(15) Leyer, M.; Stellmach, J.; Meissner, Ch.; Pristovsek, M.; Kneissl, M. *J. Cryst. Growth* **2008**, *310*, 4913−4915.

(16) Pereira, S.; Correia, M. R.; Pereira, E.; O'Donnell, K. P.; Trager-Cowan, C.; Sweeney, F.; Alves, E. *Phys. Rev. B* **2011**, *60*, 205311.

(17) Stringfellow, G. B. *J. Cryst. Growth* **2010**, *312*, 735−749.

(18) Pantzas, K.; Patriarche, G.; Troadec, D.; Gautier, S.; Moudakir, T.; Suresh, S.; Largeau, L.; Mauguin, O.; Voss, P. L.; Ougazzaden, A. *Nanotechnology* **2012**, *23*, 455707.

(19) Fischer, A. M.; Wu, Z.; Sun, K.; Wei, Q.; Huang, Y.; Senda, R.; Iida, D.; Iwaya, M.; Amano, H.; Ponce, F. A. *Appl. Phys. Express* **2009**, *2*, 041002.

(20) Neumann, W.; Mogilatenko, A.; Wernicke, T.; Richter, E.; Weyers, M.; Kneissl, M. *J. Microsc.* **2010**, *237*, 308−313.

(21) Hugues, M.; Shields, P. A.; Sacconi, F.; Mexis, M.; Auf der Maur, M.; Cooke, M.; Dineen, M.; Di Carlo, A.; Allsopp, D. W. E.; Zúñiga-Pérez, J. *J. Appl. Phys.* **2013**, *114*, 084307.

(22) Coulon, P.-M.; Alloing, B.; Brändli, V.; Vennéguès, P.; Leroux, M.; Zúñiga-Pérez, J. *Appl. Phys. Express* **2016**, *9*, 015502.

(23) Tourbot, G.; Bougerol, C.; Glas, F.; Zagonel, L. F.; Mahfoud, Z.; Meuret, S.; Gilet, P.; Kociak, M.; Gayral, B.; Daudin, B. *Nanotechnology* **2012**, *23*, 135703.

(24) Woo, S. Y.; Bugnet, M.; Nguyen, H. P. T.; Mi, Z.; Botton, G. A. *Nano Lett.* **2015**, *15*, 6413−6418.

(25) Li, S.; Waag, A. *J. Appl. Phys.* **2012**, *111*, 071101.

(26) Yanagihara, A.; Ishizawa, S.; Kishino, K. *Appl. Phys. Express* **2014**, *7*, 112102.

(27) Zhuang, Y. D.; Lewins, C. J.; Lis, S.; Shields, P. A.; Allsopp, D. W. E. *IEEE Photonics Technol. Lett.* **2013**, *25*, 1047−92013.

(28) Wierer, J. J., Jr.; Li, Q.; Koleske, D. D.; Lee, S. R.; Wang, G. T. *Nanotechnology* **2012**, *23*, 194007.

(29) Koester, R.; Hwang, J.-S.; Salomon, D.; Chen, X.; Bougerol, C.; Barnes, J.-P.; Dang; Dle, S.; Rigutti, L.; de Luna Bugallo, A.; Jacopin, G.; Tchernycheva, M.; Durand, C.; Eymery, J. *Nano Lett.* **2011**, *11*, 4839−4845.

(30) Yeh, T.-W.; Lin, Y.-T.; Stewart, L. S.; Dapkus, P. D.; Sarkissian, R.; O'Brien, J. D.; Ahn, B.; Nutt, S. R. *Nano Lett.* **2012**, *12*, 3257−3262.

(31) Liao, C.-H.; Chang, W.-M.; Yao, Y.-F.; Chen, H.-T.; Su, C.-Y.; Chen, C.-Y.; Hsieh, C.; Chen, H.-S.; Tu, C.-G.; Kiang, Y.-W.; Yang, C. C.; Hsu, T.-C. *J. Appl. Phys.* **2013**, *113*, 054315.

(32) Ra, Y. H.; Navamathavan, R.; Park, J. H.; Lee, C. R. *Nano Lett.* **2013**, *13*, 3506−3516.

(33) Le Boulbar, E. D.; Edwards, P. R.; Vajargah, S. H.; Griffiths, I.; Gîrgel, I.; Coulon, P.-M.; Cherns, D.; Martin, R. W.; Humphreys, C. J.; Bowen, C. R.; Allsopp, D. W. E.; Shields, P. A. *Cryst. Growth Des.* **2016**, *16*, 1907−1916.

(34) Shields, P. A.; Allsopp, D. W. E. *Microelectron. Eng.* **2011**, *88*, 3011.
(35) Le Boulbar, E. D.; Gîrgel, I.; Lewins, C. J.; Edwards, P. R.; Martin, R. W.; Šatka, A.; Allsopp, D. W. E.; Shields, P. A. *J. Appl. Phys.* **2013**, *114*, 094302.
(36) Lewins, C. J.; Le Boulbar, E. D.; Lis, S. M.; Edwards, P. R.; Martin, R. W.; Shields, P. A.; Allsopp, D. W. E. *J. Appl. Phys.* **2014**, *116*, 044305.
(37) Lu, P. F.; Sun, C.; Cao, H. W.; Ye, H.; Zhong, X. X.; Yu, Z. Y.; Han, L. H.; Wang, S. M. *Solid State Commun.* **2014**, *178*, 1−6.
(38) Northrup, J. E.; Romano, L. T.; Neugebauer, J. *Appl. Phys. Lett.* **1999**, *74*, 2319.
(39) Kelchner, K. M.; Kuritzky, L. Y.; Nakamura, S.; DenBaars, S. P.; Speck, J. S. *J. Cryst. Growth* **2015**, *411*, 56−62.
(40) Kaufmann, N. A. K.; Lahourcade, L.; Hourahine, B.; Martin, D.; Grandjean, N. *J. Cryst. Growth* **2016**, *433*, 36−42.
(41) Shiojiri, M.; Chuo, C. C.; Hsu, J. T.; Yang, J. R.; Saijo, H. *J. Appl. Phys.* **2006**, *99*, 073505.
(42) Richard, M.-I.; Highland, M. J.; Fister, T. T.; Munkholm, A.; Mei, J.; Streiffer, S. K.; Thompson, C.; Fuoss, P. H.; Stephenson, G. B. *Appl. Phys. Lett.* **2010**, *96*, 051911.
(43) Stankevic, T.; Mickevicius, S.; Nielsen, M. S.; Kryliouk, O.; Ciechonski, R.; Vescovi, G.; Bi, Z.; Mikkelsen, A.; Samuelson, L.; Gundlach, C.; Feidenhans'l, R. *J. Appl. Crystallogr.* **2015**, *48*, 344−349.
(44) Edwards, P. R.; Jagadamma, L. K.; Bruckbauer, J.; Liu, C.; Shields, P.; Allsopp, D.; Wang, T.; Martin, R. W. *Microsc. Microanal.* **2012**, *18*, 1212−1219.
(45) Zhuang, Y. D.; Bruckbauer, J.; Shields, P. A.; Edwards, P. R.; Martin, R. W.; Allsopp, D. W. E. *J. Appl. Phys.* **2014**, *116*, 174305.

DOI: 10.1021/acs.cgd.6b01281
Cryst. Growth Des. 2017, 17, 474−482